scientific reports

Check for updates

OPEN

Photocatalytic degradation of brilliant green and 4-nitrophenol using Ni-doped $Gd(OH)_3$ nanorods

Shaidatul Najihah Matussin[1], Fazlurrahman Khan[2,3,4], Mohammad Hilni Harunsani[1], Young-Mog Kim[3,4,5] & Mohammad Mansoob Khan[1]✉

Gadolinium hydroxide ($Gd(OH)_3$) was synthesized via a microwave-assisted synthesis method. Nickel ion (Ni^{2+}) was doped into $Gd(OH)_3$, in which 4–12% Ni-$Gd(OH)_3$ was synthesized, to study the effect of doping. The structural, optical, and morphological properties of the synthesized materials were analyzed. The crystallite sizes of the hexagonal structure of $Gd(OH)_3$ and Ni-$Gd(OH)_3$, which were 17–30 nm, were obtained from x-ray diffraction analysis. The vibrational modes of $Gd(OH)_3$ and Ni-$Gd(OH)_3$ were confirmed using Raman and Fourier-transform infrared spectroscopies. The band gap energy was greatly influenced by Ni-doping, in which a reduction of the band gap energy from 5.00 to 3.03 eV was observed. Transmission electron microscopy images showed nanorods of $Gd(OH)_3$ and Ni-$Gd(OH)_3$ and the particle size increased upon doping with Ni^{2+}. Photocatalytic degradations of brilliant green (BG) and 4-nitrophenol (4-NP) under UV light irradiation were carried out. In both experiments, 12% Ni-$Gd(OH)_3$ showed the highest photocatalytic response in degrading BG and 4-NP, which is about 92% and 69%, respectively. Therefore, this study shows that Ni-$Gd(OH)_3$ has the potential to degrade organic pollutants.

Keywords $Gd(OH)_3$, Nickel-doped $Gd(OH)_3$, 4-nitrophenol, Brilliant green, Photocatalysis

Organic dyes have been reported to be widely found in paper, textile, and apparel industrial wastewater[1–3]. These dyes generally consist of non-biodegradable, highly poisonous, and colored pigments[4]. The dye-polluted effluents can be seen polluting aquatic environments and are harmful to living organisms[5]. Therefore, removing dyes from wastewater needs urgent attention. Furthermore, 4-nitrophenol (4-NP), among the non-colored pollutants, is known to be anthropogenic and stable in nature, which would make the mineralization or degradation of 4-NP difficult at high amounts[6]. When exposed to 4-NP, severe symptoms could develop in both human beings and animals such as vomiting, headaches, and impairment of organs[7]. Therefore, like organic dyes, removing 4-NP from the environment is crucial.

The trivalent rare-earth ions (RE^{3+}) are the most common and these materials have unique properties in terms of energy storage due to their unpaired 4*f* electrons[8,9]. Moreover, RE elements have attracted attention due to their controllable structure and excellent physical and chemical properties[8–10]. These promising materials have been used in different applications for instance, these materials are used as catalysts and luminescent materials, in sensors and detectors, and biomedical devices. Moreover, RE compounds are mainly used as fluorescence labels for bio-sensing[11–15]. RE hydroxides ($RE(OH)_3$) amongst others have gradually attracted attention and have been synthesized through various methods[16–20].

Gadolinium hydroxide ($Gd(OH)_3$) has shown to be a good magnetic resonance imaging (MRI) contrast agent. Recently, $Gd(OH)_3$ and $Gd(OH)_3$-based materials have extended their uses to computed tomography (CT) contrast agents and other applications such as photocatalysis and drug delivery[21–24]. Diverse morphologies and particle sizes of $Gd(OH)_3$ and its based materials have been prepared via different synthesis methods[20,25–28]. For instance, the synthesis of $Gd(OH)_3$ nanoclusters via precipitation method at 350 °C for 10 min was reported[29]. The effect of organic modifier, 3,4-dihydroxy hydrocinnamic acid (DHCA) in the synthesis was studied. Interestingly,

[1]Chemical Sciences, Faculty of Science, Universiti Brunei Darussalam, Jalan Tungku Link, Gadong, BE 1410, Brunei Darussalam. [2]Institute of Fisheries Science, Pukyong National University, Busan 48513, Republic of Korea. [3]Marine Integrated Biomedical Technology Center, The National Key Research Institutes in Universities, Pukyong National University, Busan 48513, Republic of Korea. [4]Research Center for Marine Integrated Bionics Technology, Pukyong National University, Busan 48513, Republic of Korea. [5]Department of Food Science and Technology, Pukyong National University, Busan 48513, Republic of Korea. ✉email: mmansoobkhan@yahoo.com; mansoob.khan@ubd.edu.bn

in the absence of DHCA, the as-prepared $Gd(OH)_3$ showed a rod-like structure with an average length between 30 and 40 nm. However, with the addition of DHCA, $Gd(OH)_3$ showed a cluster-like structure with an average length of 700–1000 nm. On the other hand, Eu-doped $Gd(OH)_3$ was also synthesized using a precipitation method[30]. Hexagonal microprism morphology with a length of 0.09–0.15 µm was obtained. The synthesis of Fe-doped $Gd(OH)_3$ via hydrothermal reaction produced a rod-like morphology of Fe-doped $Gd(OH)_3$[31]. Moreover, Ullah et al. synthesized Pd@$Gd(OH)_3$ through hydrothermal method at 180 °C for 12 h[32]. Rod-like morphology of Pd@$Gd(OH)_3$ was observed to be 100–200 nm in length and 30 nm in diameter. Au@$Gd(OH)_3$ was also successfully synthesized through the hydrothermal route[25]. The synthesized Au@$Gd(OH)_3$ exhibited rod-like morphology with 150 nm in length and 17 nm in diameter.

In this paper, $Gd(OH)_3$ and Ni-$Gd(OH)_3$ NRs were synthesized using a microwave-assisted synthesis method. To the best of the authors' knowledge, no report on the microwave-assisted synthesis of $Gd(OH)_3$ and Ni-$Gd(OH)_3$ has been reported. The structural, optical, and morphological properties of $Gd(OH)_3$ and Ni-$Gd(OH)_3$ NRs were investigated using various techniques. Furthermore, the photocatalytic degradation of 4-NP and brilliant green (BG) by using $Gd(OH)_3$ and (4, 8, and 12%) Ni-$Gd(OH)_3$ under UV light irradiation was studied.

Experimental

Chemicals used

Gadolinium nitrate hexahydrate ($Gd(NO_3)_3{\cdot}6H_2O$, 99%) and nickel nitrate hexahydrate ($Ni(NO_3)_2{\cdot}6H_2O$, 99%) were obtained from Sigma-Aldrich. Sodium hydroxide (NaOH, 99.9%) was obtained from Merck. Water was purified using aquatron (England) and used throughout the experiments. For photocatalysis experiments, brilliant green ($C_{27}H_{34}N_2O_4S$, 90%) and 4-nitrophenol ($C_6H_5NO_3$, 99%) were used and obtained from Merck and Sigma-Aldrich, respectively.

Instruments used

The synthesis of $Gd(OH)_3$ and Ni-$Gd(OH)_3$ was carried out using a microwave reactor (Anton Paar Monowave 400, Austria). X-ray diffractometer (XRD) with Cu Kα radiation (λ = 1.5418 Å) (Shimadzu XRD-7000), Fourier Transform-Infrared Spectroscopy (FT-IR, Shimadzu IRPrestige-21 Fourier Transform-Infrared Spectrophotometer), Raman spectrometer (NRS-5100, JASCO) and X-ray photoelectron spectroscopy (XPS, Kratos Analytical, AXIS Nova) were used to analyze the structural properties of $Gd(OH)_3$ and Ni-$Gd(OH)_3$. The estimation of the band gap energies of $Gd(OH)_3$ and Ni-$Gd(OH)_3$ was conducted using UV–Vis DRS spectroscopy (Shimadzu, UV-2600). The morphology was analyzed using field emission transmission electron microscopy (FE-TEM) and selected area electron diffraction (SAED) conducted with JEM-F200 (JEOL Ltd., Tokyo, Japan). Photocatalytic activities of 4-NP and BG degradation were carried out using a Toption (TOPT-V) photochemical reactor irradiated by a 300 W UV lamp and the absorbance of 4-NP and BG was monitored using UV–visible spectrophotometer (Shimadzu UV-1900, Japan).

Microwave-assisted synthesis of $Gd(OH)_3$ NRs

$Gd(OH)_3$ NRs were synthesized using the microwave-assisted synthesis method. In brief, 15 mL of 0.05 M of $Gd(NO_3)_3{\cdot}6H_2O$ aqueous solution was prepared in a microwave vessel. Next, 2.4 mL of 1 M NaOH was added dropwise into the solution. The pH of the solution was about 10. The vessel was then put in the microwave reactor in which the temperature was increased in a step-wise manner; from room temperature to 90 °C and finally to 180 °C. The temperature was maintained at 180 °C for 15 min at 850 W microwave power. Once the precipitate was formed, it was then centrifuged and washed three times with water before drying at 80 °C.

Microwave-assisted synthesis of Ni-$Gd(OH)_3$ NRs

Ni-$Gd(OH)_3$ NRs were synthesized using the same method as mentioned above. A 15 mL of 0.05 M aqueous $Gd(NO_3)_3{\cdot}6H_2O$ solution was prepared and a specific amount of $Ni(NO_3)_2{\cdot}6H_2O$ was added to prepare 4, 8, and 12% Ni-$Gd(OH)_3$ NRs. NaOH with a concentration of 1 M was then added dropwise into the solution and the pH of the solution was about 10. Subsequently, the synthesis reaction was heated in a step-wise manner to 90 °C and finally to 180 °C and maintained at 180 °C for 15 min at 850 W microwave power. The precipitate was then centrifuged and washed three times with distilled water before it was dried at 80 °C. The products were coded as 4% Ni-$Gd(OH)_3$, 8% Ni-$Gd(OH)_3$, and 12% Ni-$Gd(OH)_3$.

Photocatalytic degradation of brilliant green and 4-nitrophenol

Photocatalytic degradation of BG dye and 4-NP using $Gd(OH)_3$ and 4, 8, and 12% Ni-$Gd(OH)_3$ NRs under UV light irradiation were investigated. In brief, 10 mg of $Gd(OH)_3$ and 4, 8, and 12% Ni-$Gd(OH)_3$ NRs were mixed with 50 mL of the respective pollutants: 10 ppm of BG dye or 4-NP solutions. The sample mixture was sonicated for 3 min and stirred in the dark for another 3 min. Then, the reaction solutions were continuously stirred and irradiated with UV light (300 W) for 5 h. The absorbance of the BG or 4-NP solution at λ_{max} of 620 and 316 nm, respectively, was taken every 1 h to observe the photocatalysis progress for a total of five hours. The percentage of photocatalytic BG dye or 4-NP degradation was obtained using the following equation (Eq. 1):

$$\%photocatalytic\ BG\ dye\ or\ 4-NP\ degradation = \frac{(A_{blank} - A_{sample})}{A_{blank}} \times 100 \quad (1)$$

where A_{blank} is the absorbance of BG or 4-NP only and A_{sample} is the absorbance of BG or 4-NP after photocatalytic degradation reaction with the respective catalyst.

Results and discussion

X-ray diffraction and Fourier Transform infrared spectroscopy

XRD analysis of $Gd(OH)_3$ and Ni-$Gd(OH)_3$ NRs was conducted and the XRD patterns are presented in Fig. 1a. Pure $Gd(OH)_3$ showed a hexagonal phase with a space group of $P6_3/m$ and the peaks at $2\theta = 16.22$, 28.07, 29.53, 32.75, and 37.68° are associated with (010), (110), (011), (020), and (111) planes, respectively (JCPDS 98-020-0093)[33]. No additional peaks were observed after doping with Ni^{2+} ions, suggesting the successful incorporation of Ni^{2+} into the $Gd(OH)_3$ lattice. Figure 1b shows the zoom-in view of the (010) plane of $Gd(OH)_3$ and Ni-$Gd(OH)_3$. No significant shift was observed with Ni-doping which suggests that the Ni-doping did not change the $Gd(OH)_3$ lattice. However, the peak intensity was seen to decrease. This might be due to the reduction in the crystallinity of $Gd(OH)_3$[34].

The effect of Ni doping on the structural properties of $Gd(OH)_3$ was studied by the estimation of the average crystallite sizes of $Gd(OH)_3$ and Ni-$Gd(OH)_3$ using the Debye–Scherrer's equation (Eq. 2) and their average lattice strains were also calculated (Eq. 3)[7,35]:

$$D = k\lambda/\beta \cos\theta \tag{2}$$

$$\varepsilon = \frac{\beta_{hkl}}{4tan\theta} \tag{3}$$

where λ represents the wavelength of the x-ray, θ indicates Bragg's angle, and β is the full width at half maximum of the characteristic peaks. The calculated average crystallite size of $Gd(OH)_3$ was found to be 30.08 nm (Table 1). When 4% Ni was doped into $Gd(OH)_3$, the average crystallite size was reduced to 20.84 nm. Further doping showed similar crystallite size (21.59 nm) for 8% Ni-$Gd(OH)_3$. However, 12% Ni-$Gd(OH)_3$ showed smaller crystallite size of 17.34 nm. However, the lattice parameters and cell volumes of $Gd(OH)_3$ and Ni-$Gd(OH)_3$ show insignificant change. Nonetheless, the average lattice strain increased with Ni-doping from 0.0012 to 0.0021. The Ni-doping has mainly influenced the average crystallite size and the lattice strain. However, the Ni-doping was observed to maintain the $Gd(OH)_3$ lattice without significantly affecting the lattice parameter and the cell volume.

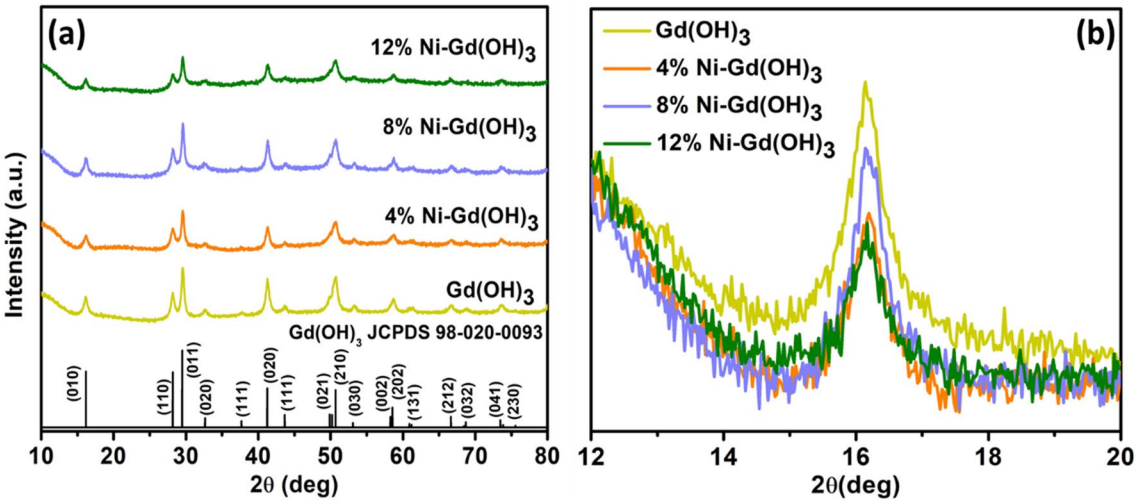

Figure 1. (**a**) XRD pattern and (**b**) zoom-in view of the (010) plane of $Gd(OH)_3$ and 4, 8, and 12% Ni-$Gd(OH)_3$ NRs.

Samples	Average crystallite size (nm)	Lattice parameter (Å)		Cell volume (Å^3)	Average lattice strain (ε)
		a	*c*		
$Gd(OH)_3$	30.08	6.34	4.18	145.51	0.0012
4% Ni-$Gd(OH)_3$	20.84	6.32	4.18	144.59	0.0017
8% Ni-$Gd(OH)_3$	21.59	6.31	4.18	144.13	0.0019
12% Ni-$Gd(OH)_3$	17.34	6.31	4.18	144.13	0.0021

Table 1. Average crystallite size (nm), lattice parameter (Å), cell volume (Å^3), and lattice strain(ε) of $Gd(OH)_3$ and Ni-$Gd(OH)_3$ NRs.

Fourier transform infrared spectroscopy and Raman spectroscopy

Figure 2(a) shows the FT-IR spectra of $Gd(OH)_3$ and Ni-$Gd(OH)_3$ NRs. All samples showed a bending vibration of Gd–O–H in the range of 600–750 cm^{-1}, which confirmed the synthesis of $Gd(OH)_3$ and Ni-$Gd(OH)_3$. The common symmetric and asymmetric stretching of O–C–O in $Gd(OH)_3$ can be observed in the range of 1370–1530 cm^{-1}[136]. The O–H vibration band and the stretching and bending of O–H vibration were observed at ~ 1600 cm^{-1} and ~ 3500 cm^{-1}, respectively[37]. Raman spectra of $Gd(OH)_3$, 4%, 8%, and 12% Ni-$Gd(OH)_3$ are shown in Fig. 2b. Pure $Gd(OH)_3$ showed three main Raman peaks assigned to A_g translatory, E_{2g} translatory, and E_{1g} liberation modes which are located at 308.85, 387.34, and 490.52 cm^{-1}, respectively[37]. One should note that, $4A_g$, $2E_{1g}$, and $5E_{2g}$ are known to be Raman active for hexagonal phase $Gd(OH)_3$ with $P6_3/m$ space group[37]. The Raman peak intensity was decreased when 4% Ni was doped into $Gd(OH)_3$. Expectedly, when more Ni-doping was incorporated the Raman peak intensity decreased further. This suggests that with more Ni-doping, the distortion of the lattice periodicity and long-range translational crystal symmetry caused by the induced defects occurred in the crystal lattice[38].

Transmission electron microscopy

TEM images of $Gd(OH)_3$, 4%, 8%, and 12% Ni-$Gd(OH)_3$ are shown in Fig. 3a_1–d_1, and all synthesized materials displayed rod-like morphology. This indicates that the addition of Ni-doping has no major influence on the

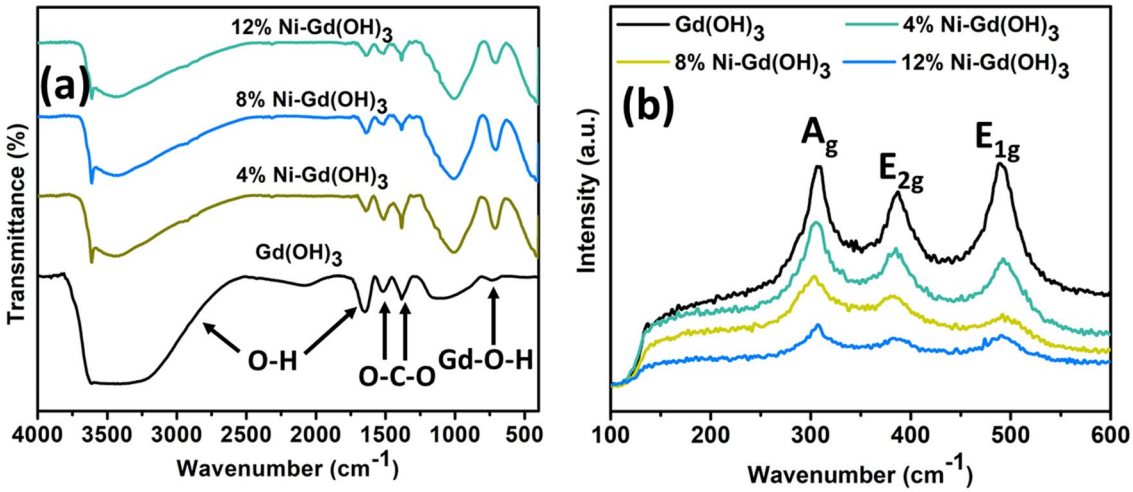

Figure 2. (**a**) FT-IR and (**b**) Raman spectra of $Gd(OH)_3$ and 4, 8, and 12% Ni-$Gd(OH)_3$ NRs.

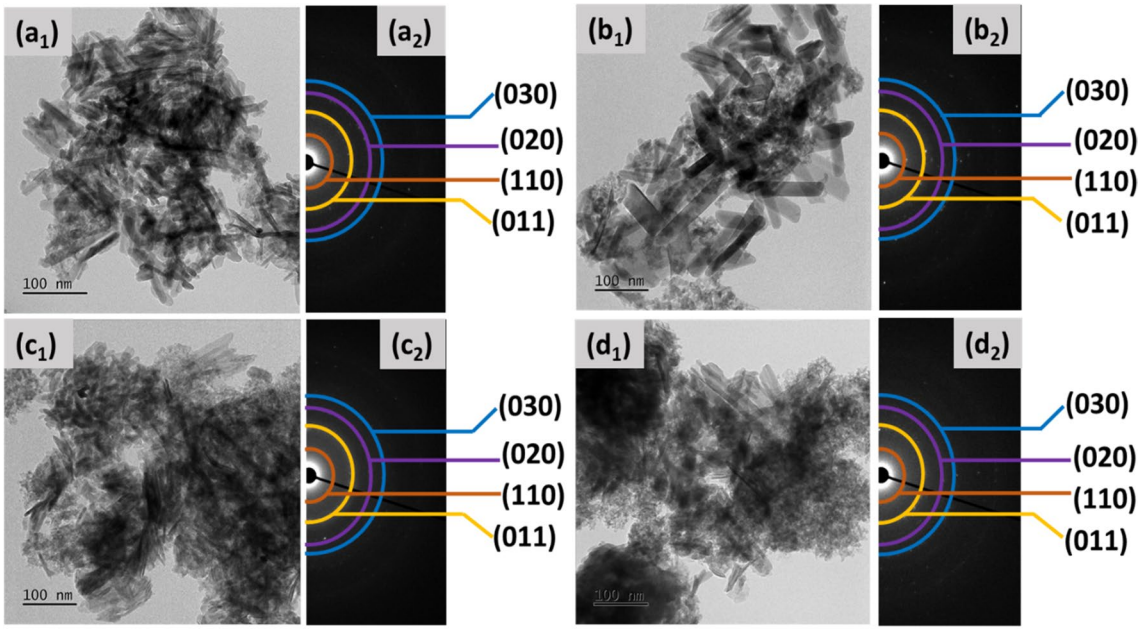

Figure 3. TEM images of (**a_1**) $Gd(OH)_3$, (**b_1**) 4% Ni-$Gd(OH)_3$, (**c_1**) 8% Ni-$Gd(OH)_3$, and (**d_1**) 12% Ni-$Gd(OH)_3$ and SAED patterns of (**a_2**) $Gd(OH)_3$, (**b_2**) 4% Ni-$Gd(OH)_3$, (**c_2**) 8% Ni-$Gd(OH)_3$, and (**d_2**) 12% Ni-$Gd(OH)_3$.

morphology. However, the particle size was influenced by the Ni doping. $Gd(OH)_3$ showed an average length of 38 nm and a diameter of 12 nm (Table 2). When 4% Ni was incorporated, the particle length was increased to 76 nm and the diameter was increased to 26 nm. This suggests that Ni-doping has some influence on the particle size of $Gd(OH)_3$ as reported by Kumar et al.[39] However, further increase in Ni doping has no more influence on the particle lengths. The average particle lengths for 8% Ni-$Gd(OH)_3$ and 12% Ni-$Gd(OH)_3$ were 76 nm and 75 nm and the average diameters were 13 and 14 nm, respectively. This might be due to the hindering of crystal growth at a certain level of doping, in which, in this case, 12% Ni might hinder the crystal growth[40].

The phase and diffraction patterns of $Gd(OH)_3$, 4%, 8%, and 12% Ni-$Gd(OH)_3$ NRs were examined by SAED analysis as shown in Figs. $3a_2$–d_2. It was observed that the synthesized materials exhibit four broad rings, which are attributed to the (110), (011), (020), and (030) reflections of the hexagonal $Gd(OH)_3$ ($P6_3/m$) structure. This is in agreement with the XRD results (Section "X-ray diffraction and Fourier Transform Infrared spectroscopy").

UV–vis diffuse reflectance spectroscopy

The band gap energy of $Gd(OH)_3$ and Ni-$Gd(OH)_3$ was estimated from the Tauc plot (Fig. 4) that was obtained from the Kubelka–Munk equation (Eq. 4).

$$F(R) = \left(\frac{(1-R)^2}{2R} \times h\nu\right)^{\frac{1}{2}} \tag{4}$$

where R is the measured absolute reflectance of the samples. The band gap can be obtained from the plots of $[F(R)h\nu]^{1/2}$ versus $h\nu$.

The band gap energy of pure $Gd(OH)_3$ is 5.00 eV which is in good agreement with literature[41]. Interestingly, the band gap energy decreased to 4.37 eV in the case of 4% Ni-$Gd(OH)_3$. This suggests that the Ni-doping has affected the optical band gap energy of $Gd(OH)_3$. Further increase in the percentage of Ni-doping has led to a decrease in the band gap energy even further. Therefore, 8% Ni-$Gd(OH)_3$ and 12% Ni-$Gd(OH)_3$ showed band gap energies of 3.75 and 3.03 eV. The band gap energies of all samples were tabulated in Table 2.

Sample	Average particle size (nm) from TEM	Band gap energy (eV)
$Gd(OH)_3$	38 (L), 12 (D)	5.00
4% Ni-Gd $(OH)_3$	76 (L), 26 (D)	4.37
8% Ni-Gd $(OH)_3$	76 (L), 13 (D)	3.75
12% Ni-Gd $(OH)_3$	75 (L), 14 (D)	3.03

Table 2. Average particle sizes from TEM and the band gap energy of $Gd(OH)_3$, and Ni-$Gd(OH)_3$ NRs (*L = length and D = diameter).

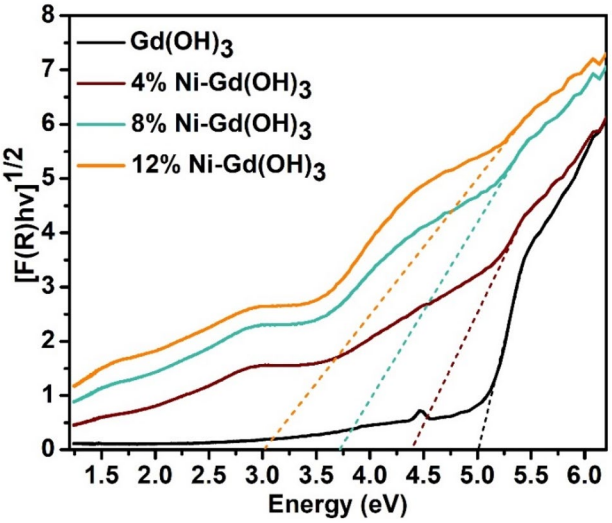

Figure 4. Tauc plot obtained from the Kubelka–Munk function for band gap energy estimation of $Gd(OH)_3$ and 4, 8, and 12% Ni-$Gd(OH)_3$ NRs.

X-ray photoelectron spectroscopy

The chemical state and the electronic structure of the elements in $Gd(OH)_3$ and Ni-$Gd(OH)_3$ were analyzed using XPS. Figure 5a shows the survey scan spectra of the synthesized materials confirming the presence of Gd 4*d*, Ni 2*p*, and O 1*s*. The Gd 4*d* core level peak is shown in Fig. 5b. Two major peaks at approximately 140.3 and 146.1 eV were observed, corresponding to Gd^{3+} $4d_{3/2}$ and Gd^{3+} $4d_{5/2}$, respectively[32]. No peak shift was observed for all the synthesized materials. Figure 5c shows the XPS spectra of two prominent Ni 2*p* peaks of 4% Ni-$Gd(OH)_3$, 8% Ni-$Gd(OH)_3$ and 12% Ni-$Gd(OH)_3$ NRs. The two prominent peaks at 853.9 and 871.6 eV correspond to the Ni $2p_{3/2}$ and Ni $2p_{1/2}$, respectively[42]. Furthermore, the peak intensity was increased with more Ni-doping. The peak positions of 878.7 and 860.4 eV represent Ni $2p_{3/2}$ and Ni $2p_{1/2}$ satellite peaks[43].

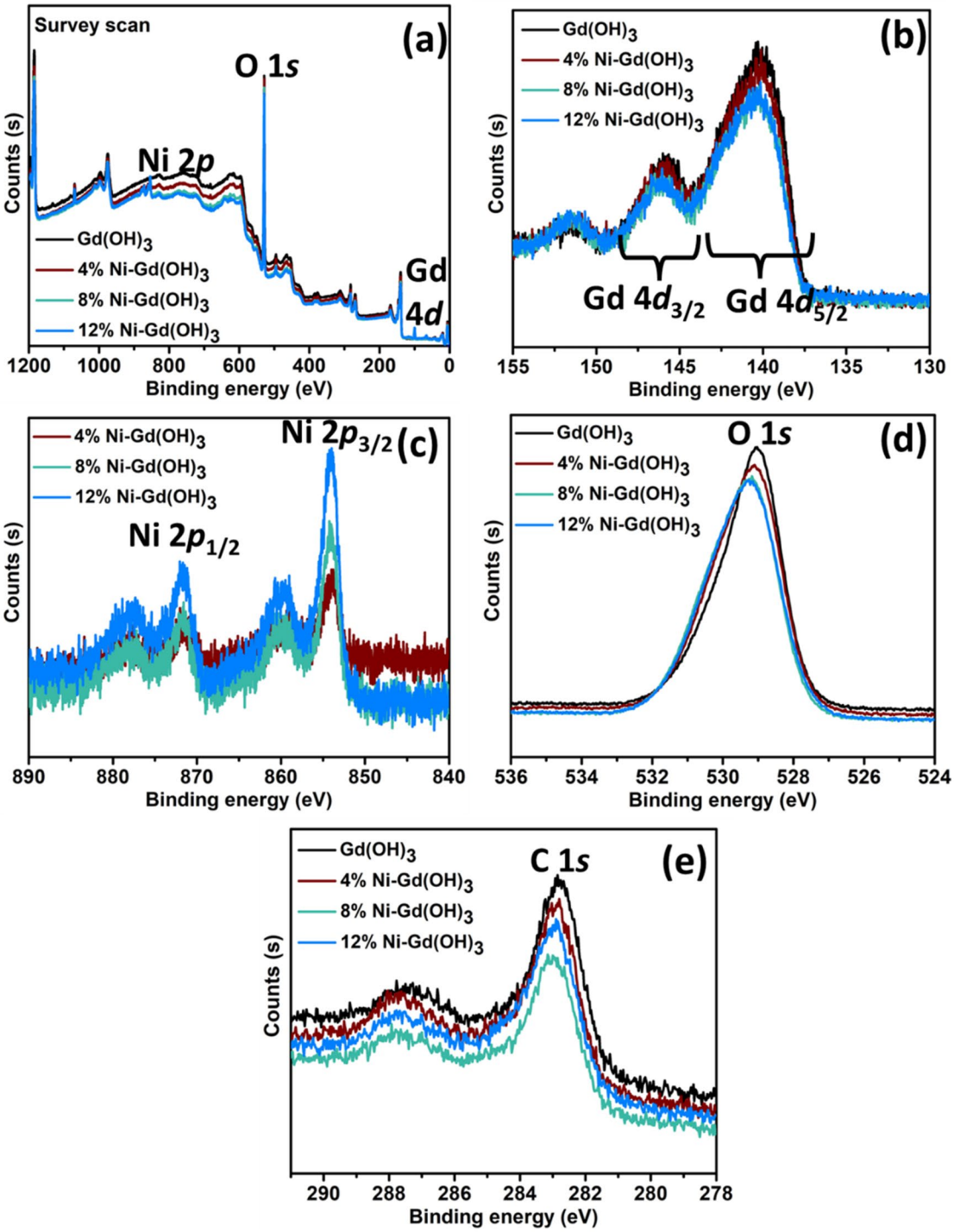

Figure 5. XPS spectra of $Gd(OH)_3$ and Ni-$Gd(OH)_3$ NRs: (**a**) Survey scan, (**b**) Gd 4*d*, (**c**) Ni 2*p*, (**d**) O 1*s*, and (**e**) C 1*s*.

The XPS spectrum of O 1*s* can be seen in Fig. 5d, in which all the samples exhibit one major peak. The peak at approximately 529.0 eV indicates the OH^- anion[44]. Slight shifts and changes in the peak position and intensity were observed for Ni-$Gd(OH)_3$. The typical C 1*s* peaks at 282.9 eV were observed in the spectra (Fig. 5e). XPS intensities were observed to vary with the incorporation of Ni^{2+} ions. The atomic concentrations of C 1*s*, O 1*s*, Gd 4*d*, and Ni 2*p* are listed in Table 3.

Applications

Photocatalytic degradation of BG dye

The photocatalytic degradation of BG using $Gd(OH)_3$ and Ni-$Gd(OH)_3$ was studied under the irradiation of UV light for 5 h (Fig. 6). The progress of the photocatalytic activity was monitored every hour by measuring the absorbance of the treated BG solution at $\lambda_{max} = 620$ nm. The experiment was conducted in triplicates and the average percentage of the photocatalysis is shown in Fig. 6a.

At the 1st and 2nd hour, $Gd(OH)_3$ showed no photocatalytic response but there was a slight response at the 3rd and 4th hour. It was finally able to degrade about 14.81 ± 1.96% at the 5th hour of UV light irradiation. 4% Ni-$Gd(OH)_3$ showed a slightly better photocatalytic response even though it was only able to degrade less than 30% from 1st to 4th hour. It finally degraded about 37.82 ± 0.51% of BG at the 5th hour. The photocatalytic response was seen increasing with more Ni-doping, as can be observed from 8% Ni-$Gd(OH)_3$. At the 1st hour, 8% Ni-$Gd(OH)_3$ degraded about 18.35 ± 0.39% and showed about 61.39 ± 0.47% degradation at the 5th hour. Moreover, the percentage photocatalytic degradation of BG was observed to be higher for 12% Ni-$Gd(OH)_3$, which showed about 50.20 ± 2.28% at the 1st hour and 92.14 ± 0.29% at the 5th hour. This suggests that, when more Ni^{2+} was doped, the photocatalytic degradation of BG increased. Based on their band gap energies, more Ni doping resulted in the reduction of the band gap energy (i.e., 5.00–3.30 eV). The doping might help in creating defect states in the band gap which enables UV light absorption and thus inhibits rapid charge carrier recombination[45]. Table 4 shows the average percentage of the photocatalytic degradation of BG using $Gd(OH)_3$ and 4, 8, and 12% Ni-$Gd(OH)_3$ NRs.

Moreover, the photocatalytic activity of $Gd(OH)_3$ and Ni-$Gd(OH)_3$ NRs against BG was studied by applying the pseudo-first-order reactions (Eq. 5):

$$ln\frac{C_0}{C} = Kt \tag{5}$$

The rate constant of the first order (K) is expressed in 1/h. Figure 6b presents the pseudo-first-order reactions of the photocatalytic degradation of BG activity of $Gd(OH)_3$ and Ni-$Gd(OH)_3$ NRs. The rate constants of $Gd(OH)_3$, 4% Ni-$Gd(OH)_3$, 8% Ni-$Gd(OH)_3$, and 12% Ni-$Gd(OH)_3$ NRs were estimated to be 0.0226, 0.0812,

Samples	Atomic concentrations (%)			
	C 1*s*	O 1*s*	Gd 4*d*	Ni 2*p*
$Gd(OH)_3$	7.6	86.5	5.0	–
4% Ni-$Gd(OH)_3$	6.7	85.2	4.7	2.9
8% Ni-$Gd(OH)_3$	5.7	84.7	4.4	4.7
12% Ni-$Gd(OH)_3$	6.4	82.9	4.2	6.0

Table 3. The atomic concentration of C 1*s*, O 1*s*, Gd 4*d*, and Ni 2*p* of $Gd(OH)_3$ and Ni-$Gd(OH)_3$ NRs.

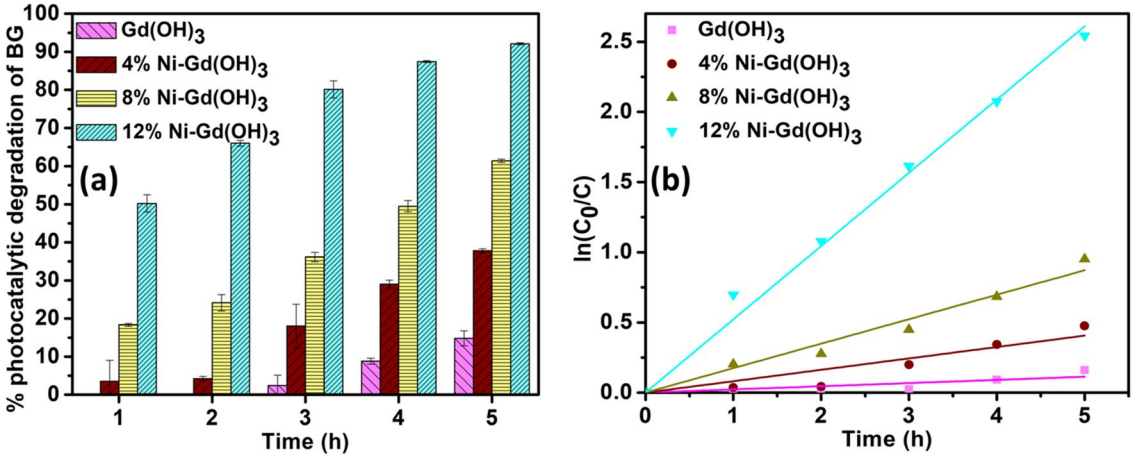

Figure 6. (**a**) Average percentage and (**b**) $\ln(C_0/C)$ plot of photocatalytic degradation of BG using $Gd(OH)_3$ and Ni-$Gd(OH)_3$ NRs under UV light irradiation.

	% photocatalytic degradation of BG				
	1 h	2 h	3 h	4 h	5 h
$Gd(OH)_3$	–	–	2.40 ± 1.71	8.82 ± 0.79	14.81 ± 1.96
4% Ni-Gd $(OH)_3$	3.53 ± 2.51	4.23 ± 0.61	18.04 ± 5.73	29.02 ± 1.07	37.82 ± 0.51
8% Ni-Gd $(OH)_3$	18.35 ± 0.39	24.13 ± 2.16	36.16 ± 1.23	49.48 ± 1.49	61.39 ± 0.47
12% Ni-Gd $(OH)_3$	50.20 ± 2.28	66.01 ± 0.77	80.11 ± 2.24	87.43 ± 0.24	92.14 ± 0.29

Table 4. The average percentage of photocatalytic activities of $Gd(OH)_3$ and 4, 8, and 12% Ni-$Gd(OH)_3$ NRs for BG degradation under UV light irradiation.

0.1744, and 0.5220 h^{-1}, respectively. It was observed that 12% Ni-$Gd(OH)_3$ NRs showed the highest reaction rate constant.

Photocatalytic degradation of 4-nitrophenol

Photocatalytic degradation of 4-NP was also investigated using $Gd(OH)_3$ and Ni-$Gd(OH)_3$ NRs under the irradiation of UV light (Fig. 7a). Similarly, at every hour, the absorbance of the treated 4-NP solution was taken and measured to observe the photocatalytic response. The readings were taken three times to ensure repeatability.

Under the UV light irradiation, the photocatalytic response of $Gd(OH)_3$ throughout the experiment was expected. It showed the lowest response amongst the samples which was about 62.74 ± 2.44% of the photocatalytic degradation of 4-NP. This might be due to its wide band gap (5.00 eV). When 4% Ni was doped, the photocatalytic response was increased slightly (63.69 ± 1.99%), suggesting the effect of Ni^{2+} doping. Moreover, the reduction in the band gap energy from 5.00 eV to 4.37 eV might cause a slight enhancement in the separation of the photogenerated electrons (e^-) and holes (h^+). Further increase in the percentage of Ni^{2+} doping has shown better photocatalytic degradation of 4-NP. In the case of 8% Ni-$Gd(OH)_3$, the overall photocatalytic response was about 67.67 ± 0.95% whereas 12% Ni-$Gd(OH)_3$ showed about 69.32 ± 1.25% of 4-NP degradation (Table 5). The band gap energies of both materials decreased with more Ni^{2+} doping, which were about 3.75 and 3.03 eV, respectively. Therefore, the efficient photocatalytic response might be due to their lower band gap energies.

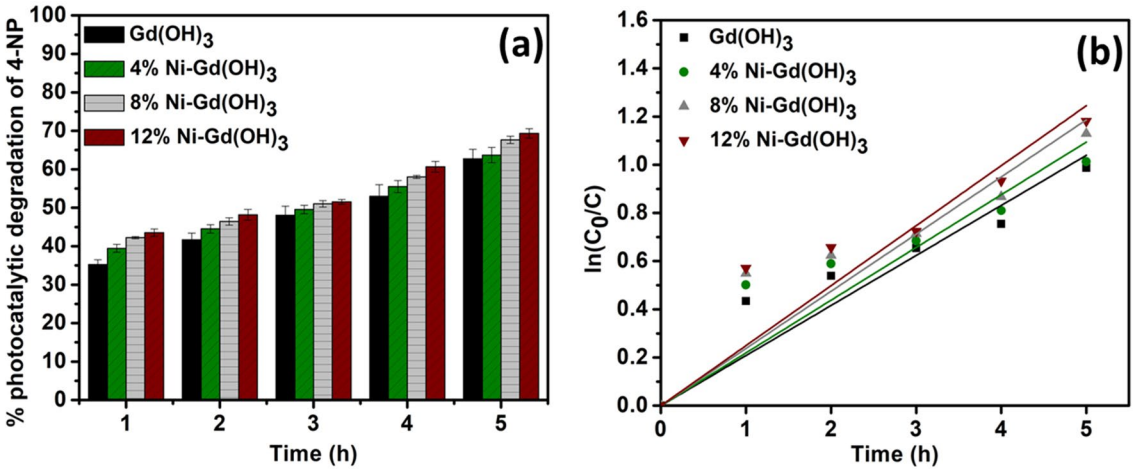

Figure 7. (**a**) Average percentage and (**b**) $\ln(C_0/C)$ plot of photocatalytic degradation of 4-NP using $Gd(OH)_3$ and Ni-$Gd(OH)_3$ NRs under UV light irradiation.

	% Photocatalytic degradation of 4-NP				
	1 h	2 h	3 h	4 h	5 h
Gd $(OH)_3$	35.22 ± 1.25	41.67 ± 1.73	48.03 ± 2.39	52.98 ± 3.03	62.74 ± 2.44
4% Ni-Gd $(OH)_3$	39.45 ± 1.02	44.52 ± 1.09	49.55 ± 1.08	55.52 ± 1.57	63.69 ± 1.99
8% Ni-Gd $(OH)_3$	42.24 ± 0.29	46.41 ± 0.96	51.03 ± 0.82	58.00 ± 0.39	67.67 ± 0.95
12% Ni-Gd $(OH)_3$	43.52 ± 0.95	48.16 ± 1.42	51.52 ± 0.62	60.66 ± 1.41	69.32 ± 1.25

Table 5. The average percentage of photocatalytic activities of $Gd(OH)_3$ and 4, 8, and 12% Ni-$Gd(OH)_3$ NRs for 4-NP degradation under UV light irradiation.

The kinetic study was conducted based on the photocatalytic activity of $Gd(OH)_3$ and Ni-$Gd(OH)_3$ NRs against 4-NP (Eq. 5). Figure 7b presents the pseudo-first-order reactions of the photocatalytic degradation of BG activity of $Gd(OH)_3$ and Ni-$Gd(OH)_3$ NRs. The rate constants of $Gd(OH)_3$, 4% Ni-$Gd(OH)_3$, 8% Ni-$Gd(OH)_3$, and 12% Ni-$Gd(OH)_3$ NRs were estimated to be 0.2078, 0.2189, 0.2374, and 0.2490 h^{-1}, respectively. It was observed that, with Ni-doping, the reaction rates were increased, and 12% Ni-$Gd(OH)_3$ NRs showed the highest reaction rate constant.

Therefore, based on both photocatalysis experiments, 12% Ni-$Gd(OH)_3$ showed the highest photocatalytic degradation of BG and 4-NP. The difference in the effectiveness of 12% Ni-$Gd(OH)_3$ in both cases might be due to the nature of the two compounds. Moreover, the narrow band gap energy of 12% Ni-$Gd(OH)_3$ (3.03 eV) might absorb UV light more efficiently and can photogenerate e^-/h^+ pairs effectively. One study reported on the catalytic photodegradation of Congo red using lanthanide hydroxides (Ln = Nd, Sm, Eu, Gd, Tb, and Dy)[46]. The removal efficiencies of $Ln(OH)_3$ are more than 90% after 1800 min. However, this current study shows improved photocatalytic efficiency where the photocatalytic degradation of BG using Ni-$Gd(OH)_3$ showed a degradation of BG over 90% in 5 h. This might be also due to the recombination of the photogenerated e^-/h^+ pairs being hindered. The photogenerated e^-/h^+ pairs would react with adsorb O_2 and H_2O to form $O_2^{\bullet-}$ and $OH^\bullet$ radicals, respectively. In general, these radicals are responsible for the degradation of pollutants. However, based on the literature, $O_2^{\bullet-}$ radicals are mainly responsible for the degradation of dyes, whereas $OH^\bullet$ radicals are responsible for the degradation of 4-NP[47–49]. Therefore, the difference in the response of 12% Ni-$Gd(OH)_3$ in the degradation of BG and 4-NP might be due to these radicals. The role of $O_2^{\bullet-}$ radicals might be more prominent during the photocatalytic degradation of BG and in the case of the photocatalytic degradation of 4-NP, $OH^\bullet$ radicals might be the more reactive species.

Conclusions

$Gd(OH)_3$ and Ni-$Gd(OH)_3$ NRs were successfully synthesized using the microwave-assisted synthesis method. The properties of the synthesized materials such as the structural, optical, and morphological properties, were analyzed using different instruments. The hexagonal structure of $Gd(OH)_3$ and Ni-$Gd(OH)_3$ with average crystallite sizes between 17 and 30 nm was obtained from XRD. The presence of the vibrational bands of $Gd(OH)_3$ and Ni-$Gd(OH)_3$ was confirmed by Raman and FT-IR spectroscopies. The band gap energy of $Gd(OH)_3$ and Ni-$Gd(OH)_3$ were reduced with Ni-doping in which the values decreased from 5.00 to 3.03 eV. TEM images showed nanorod-shaped $Gd(OH)_3$ and Ni-$Gd(OH)_3$ with increased particle size when doping with Ni^{2+}. Photocatalytic degradations of 4-NP and BG under UV light irradiation were carried out and 12% Ni-$Gd(OH)_3$ showed the highest photocatalytic response which is about 92% and 69%, respectively. Therefore, Ni-$Gd(OH)_3$ is a promising material for the degradation of organic pollutants.

Data availability

All data generated or analyzed during this study are included in the manuscript.

Received: 14 January 2024; Accepted: 2 April 2024
Published online: 09 April 2024

References

1. Chiu, Y.-H., Chang, T.-F., Chen, C.-Y., Sone, M. & Hsu, Y.-J. Mechanistic insights into photodegradation of organic dyes using heterostructure photocatalysts. *Catalysts* **9**(5), 430. https://doi.org/10.3390/catal9050430 (2019).
2. Thambiraj, S., Sharmila, G. & Ravi Shankaran, D. Green adsorbents from solid wastes for water purification application. *Mater. Today Proc.* **5**(8), 16675–16683. https://doi.org/10.1016/j.matpr.2018.06.029 (2018).
3. Khan, M. M., Rahman, A. & Matussin, S. N. Recent progress of metal-organic frameworks and metal-organic frameworks-based heterostructures as photocatalysts. *Nanomaterials* **12**(16), 2820. https://doi.org/10.3390/nano12162820 (2022).
4. Matussin, S. N., Khan, F., Harunsani, M. H., Kim, Y.-M. & Khan, M. M. Effect of Pd-doping concentrations on the photocatalytic, photoelectrochemical, and photoantibacterial properties of CeO2. *Catalysts* **13**(1), 96. https://doi.org/10.3390/catal13010096 (2023).
5. Rafiq, A. *et al.* Photocatalytic degradation of dyes using semiconductor photocatalysts to clean industrial water pollution. *J. Ind. Eng. Chem.* **97**, 111–128. https://doi.org/10.1016/j.jiec.2021.02.017 (2021).
6. Matussin, S. N., Khan, F., Harunsani, M. H., Kim, Y.-M. & Khan, M. M. Visible-light-induced photocatalytic and photoantibacterial activities of co-doped CeO $_2$. *ACS Omega* **8**(13), 11868–11879. https://doi.org/10.1021/acsomega.2c07058 (2023).
7. Matussin, S. N., Harunsani, M. H., Tan, A. L., Cho, M. H. & Khan, M. M. Effect of Co2+ and Ni2+ Co-doping on SnO2 synthesized via phytogenic method for photoantioxidant studies and photoconversion of 4-nitrophenol. *Mater. Today Commun.* **25**(September), 101677. https://doi.org/10.1016/j.mtcomm.2020.101677 (2020).
8. Liang, S. *et al.* Rare-earth based nanomaterials and their composites as electrode materials for high performance supercapacitors: A review. *Sustain. Energy Fuels* **4**(8), 3825–3847. https://doi.org/10.1039/D0SE00669F (2020).
9. Fu, R., Ou, M., Yang, C., Hu, Y. & Yin, H. Enhanced luminescence and paramagnetic properties of Gd2O3:Tb3+ multifunctional nanoparticles by K+/Co2+ doping. *J. Lumin.* **2020**(222), 117154. https://doi.org/10.1016/j.jlumin.2020.117154 (2019).
10. Matussin, S. N., Harunsani, M. H. & Khan, M. M. CeO2 and CeO2-based nanomaterials for photocatalytic, antioxidant and antimicrobial activities. *J. Rare Earths* **41**(2), 167–181. https://doi.org/10.1016/j.jre.2022.09.003 (2023).
11. Lei, P., Feng, J. & Zhang, H. Emerging biomaterials: Taking full advantage of the intrinsic properties of rare earth elements. *Nano Today* **35**, 100952. https://doi.org/10.1016/j.nantod.2020.100952 (2020).
12. Khan, M. M. & Matussin, S. N. Sm $_2$ O $_3$ and Sm $_2$ O $_3$ -based nanostructures for photocatalysis, sensors, CO conversion, and biological applications. *Catal. Sci. Technol.* **13**(8), 2274–2290. https://doi.org/10.1039/D2CY01976K (2023).
13. Singh, P., Kachhap, S., Singh, P. & Singh, S. K. Lanthanide-based hybrid nanostructures: classification, synthesis, optical properties, and multifunctional applications. *Coord. Chem. Rev.* **472**, 214795. https://doi.org/10.1016/j.ccr.2022.214795 (2022).
14. Huang, W., Liu, Q., Chen, W., Feng, M. & Zheng, Z. Recent advances in the catalytic applications of lanthanide-oxo clusters. *Magnetochemistry* **7**(12), 161. https://doi.org/10.3390/magnetochemistry7120161 (2021).
15. Qiu, X., Xu, J., Cardoso Dos Santos, M. & Hildebrandt, N. Multiplexed biosensing and bioimaging using lanthanide-based time-gated förster resonance energy transfer. *Acc. Chem. Res.* **55**(4), 551–564. https://doi.org/10.1021/acs.accounts.1c00691 (2022).

16. Mu, Q. & Wang, Y. A simple method to prepare Ln(OH)3 (Ln = La, Sm, Tb, Eu, and Gd) nanorods using CTAB micelle solution and their room temperature photoluminescence properties. *J. Alloys Compd.* **509**(5), 2060–2065. https://doi.org/10.1016/j.jallcom.2010.10.141 (2011).
17. Ji, X., Hu, P., Li, X., Zhang, L. & Sun, J. Hydrothermal control, characterization, growth mechanism, and photoluminescence properties of highly crystalline 1D Eu(OH)3nanostructures. *RSC Adv* **10**(55), 33499–33508. https://doi.org/10.1039/d0ra04338a (2020).
18. Shih, K. Y. & Yu, S. C. Microwave-assisted rapid synthesis of Eu(Oh)3/Rgo nanocomposites and enhancement of their antibacterial activity against *Escherichia coli*. *Materials* https://doi.org/10.3390/ma15010043 (2022).
19. Lee, D., Seo, J., Valladares, L. D. L. S., Avalos Quispe, O. & Barnes, C. H. W. Magnetic and structural properties of yellow europium oxide compound and Eu(OH)3. *J. Solid State Chem.* **228**, 141–145. https://doi.org/10.1016/j.jssc.2015.04.018 (2015).
20. Kumar, P. D., Pradhan, G. K., Parida, K. M. & Singh, S. K. Facile fabrication of Gd(OH)3 nanorod/RGO composite: Synthesis, characterisation and photocatalytic reduction of Cr(VI). *Chem. Eng. J.* **255**, 78–88. https://doi.org/10.1016/j.cej.2014.06.039 (2014).
21. Xu, Y. *et al.* Layered gadolinium hydroxides for simultaneous drug delivery and imaging. *Dalton Transact.* **47**(9), 3166–3177. https://doi.org/10.1039/c7dt03729e (2018).
22. Shao, B. *et al.* Eu3+-doped layered gadolinium hydroxides as drug carriers and their bactericidal behavior. *Mater. Sci. Eng.* https://doi.org/10.1016/j.msec.2021.112213 (2021).
23. Kobayashi, Y. *et al.* Fabrication of gadolinium hydroxide nanoparticles using ion-exchange resin and their MRI property. *J. Asian Ceram. Soc.* **4**(1), 138–142. https://doi.org/10.1016/j.jascer.2016.01.005 (2016).
24. Liu, W. *et al.* The photocatalytic application of Gd(OH)3/Cd0.8Zn0.2S nanocomposites in U(VI) Reduction. *Chem. Eng. J.* https://doi.org/10.1016/j.cej.2023.143117 (2023).
25. Li, J. *et al.* A facile synthesis of size- and shape-controlled Gd(OH)3 nanoparticles and Gd(OH)3@Au core/shell nanostars. *New J. Chem.* **41**(24), 15136–15143. https://doi.org/10.1039/c7nj03482b (2017).
26. Du, Y., Xing, M., Li, Z. & Guo, W. PEGylated Gd(OH)3 nanorods as metabolizable contrast agents for computed tomography imaging. *New J. Chem.* **39**(11), 8999–9005. https://doi.org/10.1039/c5nj01980j (2015).
27. Huang, S., Liu, J., Liu, D. & Yuan, Q. Facile and large-scale synthesis of Gd(OH)3 nanorods for MR imaging with low toxicity. *New J. Chem.* **36**(6), 1335. https://doi.org/10.1039/c2nj21009f (2012).
28. Al-Mhyawi, S. R. & Abdel Salam, M. Enhancement of photocatalytic activity of Gd(OH)3 nanoparticles by Pd deposition for reduction of CO2 to methanol. *J. Photochem. Photobiol. A Chem.* **367**, 89–93. https://doi.org/10.1016/j.jphotochem.2018.08.024 (2018).
29. Singh, V. *et al.* Hydrothermal synthesis of inorganic-organic hybrid gadolinium hydroxide nanoclusters with controlled size and morphology. *Dalton Transact.* **42**(45), 16176–16184. https://doi.org/10.1039/c3dt51692j (2013).
30. Li, G., Liang, Y., Zhang, M. & Yu, D. Size-tunable synthesis and luminescent properties of Gd(OH) 3:Eu3+ and Gd2O3:Eu3+ hexagonal nano-/microprisms. *CrystEngComm* **16**(29), 6670–6679. https://doi.org/10.1039/c4ce00482e (2014).
31. Zong, Y. *et al.* Hydrothermal synthesis of uniform Fe-doped Gd(OH)3 nanorods and their magnetic properties: Phase conversion from paramagnetism to ferromagnetism. *Ceram Int* **43**(10), 7881–7888. https://doi.org/10.1016/j.ceramint.2017.03.109 (2017).
32. Ullah, N. *et al.* Highly dispersed ultra-small Pd nanoparticles on gadolinium hydroxide nanorods for efficient hydrogenation reactions. *Nanoscale* **9**(36), 13800–13807. https://doi.org/10.1039/c7nr05096h (2017).
33. Beall, G. W., Milligan, W. O., Wolcott, H. A. *Structural Trends in the Lanthanide Trihydroxides*; Pergamon Press, Vol. 39; (1977).
34. Pal, M., Pal, U., Jiménez, J. M. G. Y. & Pérez-Rodríguez, F. Effects of crystallization and dopant concentration on the emission behavior of TiO2: Eu nanophosphors. *Nanoscale Res. Lett.* **7**(1), 1. https://doi.org/10.1186/1556-276X-7-1 (2012).
35. Matussin, S. N., Tan, A. L., Harunsani, M. H., Cho, M. H. & Khan, M. M. Green and phytogenic fabrication of Co-doped SnO2 using aqueous leaf extract of tradescantia spathacea for photoantioxidant and photocatalytic studies. *Bionanoscience* **11**(1), 120–135. https://doi.org/10.1007/s12668-020-00820-3 (2021).
36. Kang, J. G., Jung, Y., Min, B. K. & Sohn, Y. Full characterization of Eu(OH) 3 and Eu 2 O 3 nanorods. *Appl. Surf. Sci.* **314**, 158–165. https://doi.org/10.1016/j.apsusc.2014.06.165 (2014).
37. Kang, J. G., Min, B. K. & Sohn, Y. Synthesis and characterization of Gd(OH)3 and Gd2O3 nanorods. *Ceram. Int.* **41**(1), 1243–1248. https://doi.org/10.1016/j.ceramint.2014.09.053 (2015).
38. Komaraiah, D. *et al.* Effect of particle size and dopant concentration on the raman and the photoluminescence spectra of TiO 2: Eu 3+ nanophosphor thin films. *J. Lumin.* **211**, 320–333. https://doi.org/10.1016/j.jlumin.2019.03.050 (2019).
39. Kumar, A., Arora, M., Yadav, M. S. & Panta, R. P. Induced size effect on ni doped nickel zinc ferrite nanoparticles. *Phys. Procedia* **9**, 20–23. https://doi.org/10.1016/j.phpro.2010.11.006 (2010).
40. Bose, R., Manna, G. & Pradhan, N. Surface doping for hindrance of crystal growth and structural transformation in semiconductor nanocrystals. *J. Phys. Chem. C* **117**(40), 20991–20997. https://doi.org/10.1021/jp407123s (2013).
41. Chen, F. *et al.* Synthesis and characteristics of nanorods of gadolinium hydroxide and gadolinium oxide. *J. Alloys Compd.* **664**, 311–316. https://doi.org/10.1016/j.jallcom.2015.12.225 (2016).
42. Matussin, S. N. *et al.* Effect of Ni-doping on the properties of the SnO2 synthesized using tradescantia Spathacea for photoantioxidant studies. *Mater. Chem. Phys.* **252**, 123293. https://doi.org/10.1016/j.matchemphys.2020.123293 (2020).
43. Cheng, M., Fan, H., Song, Y., Cui, Y. & Wang, R. Interconnected hierarchical $NiCo_2O_4$ microspheres as high-performance electrode materials for supercapacitors. *Dalton Trans.* **46**(28), 9201–9209. https://doi.org/10.1039/C7DT01289F (2017).
44. Jones, T. E. *et al.* Thermodynamic and spectroscopic properties of oxygen on silver under an oxygen atmosphere. *Phys. Chem. Chem. Phys.* **17**(14), 9288–9312. https://doi.org/10.1039/C5CP00342C (2015).
45. Khaki, M. R. D., Shafeeyan, M. S., Raman, A. A. A. & Daud, W. M. A. W. Application of doped photocatalysts for organic pollutant degradation-a review. *J. Environ. Manag.* https://doi.org/10.1016/j.jenvman.2017.04.099 (2017).
46. Liu, S. *et al.* Catalytic photodegradation of congo red in aqueous solution by Ln(OH) 3 (Ln = Nd, Sm, Eu, Gd, Tb, and Dy) nanorods. *Appl. Catal A Gen.* **453**, 45–53. https://doi.org/10.1016/j.apcata.2012.12.004 (2013).
47. Verma, A., Jaihindh, D. P. & Fu, Y. P. Photocatalytic 4-nitrophenol degradation and oxygen evolution reaction in CuO/g-C3N4 composites prepared by deep eutectic solvent-assisted chlorine doping. *Dalton. Transact.* **48**(24), 8594–8610. https://doi.org/10.1039/c9dt01046g (2019).
48. Fan, Y. *et al.* Effective photodegradation of 4-nitrophenol with CuO nano particles prepared by ionic liquids/water system. *Green Chem. Eng.* **3**(1), 15–24. https://doi.org/10.1016/j.gce.2021.07.009 (2022).
49. Kang, S., Jang, J., Pawar, R. C., Ahn, S. H. & Lee, C. S. Low temperature fabrication of Fe2O3 nanorod film coated with ultra-thin g-C3N4 for a direct z-scheme exerting photocatalytic activities. *RSC Adv.* **8**(59), 33600–33613. https://doi.org/10.1039/c8ra04499f (2018).

Acknowledgements

The authors would like to acknowledge the FRC grant (UBD/RSCH/1.4/FICBF(b)/2023/059) received from Universiti Brunei Darussalam, Brunei Darussalam. This research was supported by the Basic Science Research Program through the National Research Foundation (NRF) of Korea grant funded by the Ministry of Education (2021R1A6A1A03039211 and 2022R1A2B5B01001998).

Author contributions

S.N.M.: Methodology; Investigation, Data curation; Writing – original draft. F.K.: Methodology, Investigation, Data curation. M.H.H.: Supervision, Writing – review & editing. Y.-M.K.: Resources, Formal analysis. M.M.K.: Supervision, Conceptualization, Funding acquisition, Writing – review & editing.

Competing interests

The authors declare no competing interests.

Additional information

Correspondence and requests for materials should be addressed to M.M.K.

Reprints and permissions information is available at www.nature.com/reprints.

Publisher's note Springer Nature remains neutral with regard to jurisdictional claims in published maps and institutional affiliations.